nanomaterials

MDPI

Article

Enhanced Photocurrent of the Ag Interfaced Topological Insulator Bi_2Se_3 under UV- and Visible-Light Radiations

Chih-Chiang Wang [1,2], Pao-Tai Lin [3], Fuh-Sheng Shieu [1,*] and Han-Chang Shih [1,4,*]

1 Department of Materials Science and Engineering, National Chung Hsing University, Taichung 40227, Taiwan; wilbur0913@gmail.com
2 International Agriculture Center, National Chung Hsing University, Taichung 40227, Taiwan
3 Department of Electrical and Computer Engineering, Texas A&M University, College Station, TX 77843, USA; paolin@ece.tamu.edu
4 Department of Chemical Engineering and Materials Science, Chinese Culture University, Taipei 11114, Taiwan
* Correspondence: fusshieu@dragon.nchu.edu (F.-S.S.); hcshih@mx.nthu.edu.tw (H.-C.S.)

Abstract: Bi_2Se_3 is a topological quantum material that is used in photodetectors, owing to its narrow bandgap, conductive surface, and insulating bulk. In this work, Ag@Bi_2Se_3 nanoplatelets were synthesized on Al_2O_3(100) substrates in a two-step process of thermal evaporation and magnetron sputtering. X-ray diffractometer (XRD), high-resolution transmission electron microscopy (HRTEM), Raman spectroscopy, and x-ray photoelectron spectroscopy (XPS) revealed that all samples had the typical rhombohedral Bi_2Se_3. Field-emission scanning electron microscopy (FESEM)-energy dispersive x-ray spectroscopy (EDS), XPS, and HRTEM confirmed the presence of the precipitated Ag. The optical absorptance of Bi_2Se_3 nanoplatelets in UV-visible range decreased with the Ag contents. Results of photocurrent measurements under zero-bias conditions revealed that the deposited Ag affected photosensitivity. A total of 7.1 at.% Ag was associated with approximately 4.25 and 4.57 times higher photocurrents under UV and visible light, respectively, than 0 at.% Ag. The photocurrent in Bi_2Se_3 at 7.1 at.% Ag under visible light was 1.72-folds of that under UV light. This enhanced photocurrent is attributable to the narrow bandgap (~0.35 eV) of Bi_2Se_3 nanoplatelets, the Schottky field at the interface between Ag and Bi_2Se_3, the surface plasmon resonance that is caused by Ag, and the highly conductive surface that is formed from Ag and Bi_2Se_3. This work suggests that the appropriate Ag deposition enhances the photocurrent in, and increases the photosensitivity of, Bi_2Se_3 nanoplatelets under UV and visible light.

Keywords: Bi_2Se_3; Ag; surface plasmon resonance; photocurrent

Citation: Wang, C.-C.; Lin, P.-T.; Shieu, F.-S.; Shih, H.-C. Enhanced Photocurrent of the Ag Interfaced Topological Insulator Bi_2Se_3 under UV- and Visible-Light Radiations. *Nanomaterials* **2021**, *11*, 3353. https://doi.org/10.3390/nano11123353

Academic Editors: Filippo Giannazzo and Ivan Shtepliuk

Received: 8 November 2021
Accepted: 8 December 2021
Published: 10 December 2021

1. Introduction

Bismuth selenide (Bi_2Se_3) is a material with a narrow bandgap (~0.35 eV), a rhombohedral crystal structure, a unique gapless surface state, and a bulk electronic bandgap [1–4]. The unique properties of Bi_2Se_3 arise from the time-reversal symmetry and the spin-orbit coupling, which result in high electronic conductivity at the surface (three-dimensions) and edges (two-dimensions) [5]. Bi_2Se_3 has the following favorable properties: (1) low power dissipation, (2) photon-like and spin-polarized electrons, and (3) the quantum spin Hall Effect [6–8]. Owing to its unique optoelectronic properties, Bi_2Se_3 can be used in photodetectors [9], spintronic devices [10], and topological superconductors [11,12]. Bulk Bi_2Se_3 exhibits n-type semiconducting properties owing to the Se vacancies, which supply free electrons that induce a high bulk conductivity and suppress its surface electronic transportation [13,14]. Nanosized Bi_2Se_3 crystals exhibit a weaker bulk effect and greater electronic transportation because of their high surface-to-volume ratio [15]. The methods for synthesizing nanosized Bi_2Se_3 include: (1) thermal chemical vapor deposition (CVD) process [16], (2) successive ionic layer

adsorption and reaction (SILAR) [17], (3) chemical bath deposition (CBD) [18], (4) electrodeposition [19], and (5) the solvothermal method [20]. Photodetectors are useful in optical information communications, imaging detection, and biodetection owing to the transit between photon and electron [21–23]; to be effective, they must have a high photoelectric conversion efficiency. A photodetector should (1) exhibit photo-absorptance over a wide range of wavelengths, (2) high photosensitivity, (3) high free-carrier mobility, (4) high photon-electron conversion efficiency, (5) a low operating voltage, and (6) long-term stability [24,25]. Bi_2Se_3 satisfies all of the requirements of a potential photodetector owing to its unique surface state and excellent surface electronic transportation. Various methods for enhancing its photocurrent have been reported upon. Pamu et al. found that Au or Ag nanodisks enhance the photocurrent of photosystem I (PSI) as a result of the plasmonic interaction between metal and PSI [26]. Peng et al. found that a semiconductor quantum dot of InAs/GaAs increases the photocurrent in an *n-i* Schottky device as a result of the Coulomb interaction [27]. Yan et al. found that a textured silicon wafer and periodic Ag nanoarrays increase the photocurrent of the silicon solar cell owing to their textured morphology and plasmonic effect [28]. Chakraborty et al. reported that Au increases the photocurrent in the CdSe nanowires owing to the plasmonic effect and Schottky field at the interface between the metal and the semiconductor [29]. These reports suggest that the photocurrent can be enhanced by the plasmonic effect, the Schottky field, and surface morphology. The photocurrent in, and enhancements of, Bi_2Se_3 have been studied and reported [30–32]. Wang et al. applied external strain to Bi_2Se_3 nanowires and thereby increased the photocurrent therein [33]. Gupta et al. found that the Ag nanoparticle-decorated Bi_2Se_3 that was synthesized by a chemical solution method exhibited an enhanced photocurrent at a bias of −10 V [34]. Chae et al. found that Bi_2Se_3/graphene exhibited an enhanced photocurrent with a source-drain voltage of 1.5V [35]. Liao et al. found that reduced graphene oxide increased the photocurrent of Bi_2Se_3 nanosheets [36]. Based on the enhancing factors of the plasmonic effect and the interaction between metal and semiconductors, the thermal CVD process that involves a catalyst-free vapor-solid mechanism is used herein to synthesize Bi_2Se_3 nanoplatelets, on which Ag is deposited by magnetron sputtering. The enhancement of the photocurrent in the Bi_2Se_3 nanoplatelets under UV and visible light by Ag was studied.

2. Materials and Methods

2.1. Fabrication of Pristine Bi_2Se_3 and Ag@Bi_2Se_3 Nanoplatelets

Pristine Bi_2Se_3 nanoplatelets were fabricated on an Al_2O_3 (100) substrate (0.5×0.5 mm^2) using a catalyst-free vapor-solid mechanism by thermal evaporation in a quartz tube furnace. A mixture of precursor powders of 0.1g bismuth (purity = 99%, 4.78×10^{-4} mole, Merck, Darmstadt, Germany) and 0.1g selenium (purity = 99%, 1.27×10^{-3} mole, Alfa Aesar, Ward Hill, MA, USA) were placed in an alumina boat, which was placed in the heating zone at the center of the quartz tube and heated to 600 °C at a rate of 25 °C/min under 1.5×10^{-2} Torr, in which conditions were maintained for 60 min. The Al_2O_3 (100) substrate was placed upstream in the quartz tube at about 140 °C, 21 cm away from the alumina boat. Thus, pristine Bi_2Se_3 nanoplatelets were grown on the Al_2O_3 (100) substrate. Then, the synthesized system was slowly cooled to room temperature after a 60 min deposition process. An Ag thin film was deposited on a sapphire substrate for 60 s (110V, 4 mA) at 1×10^{-1} mbar. It was then measured using a profilometer (Dektak XT, Bruker, Billerica, MA, USA) to estimate the Ag deposition rate. Then, Ag was deposited on the Bi_2Se_3 nanoplatelets at a working distance of 35 mm by magnetron sputtering (110 V, 4 mA) using a 2-inch Ag target at room temperature under 1×10^{-1} mbar. Ag was deposited for 10, 15, 20, and 25s yielding Ag10s@Bi_2Se_3, Ag15s@Bi_2Se_3, Ag20s@Bi_2Se_3, and Ag25s@Bi_2Se_3 nanoplatelets, respectively.

2.2. Characterization of Nanoplatelets

The crystal structures of the pristine Bi_2Se_3 and $Ag@Bi_2Se_3$ nanoplatelets were determined using XRD (λ = 0.154 nm, 30 A, 40 kV, Bruker D2 PHASER) at 2θ = 10–60°, and HRTEM (JEOL JEM-2010, Tokyo, Japan). XPS (PerkinElmer model PHI1600 system, Waltham, MA, USA) and Raman spectroscopy (3D Nanometer Scale Raman PL Microspectrometer, Tokyo Instruments, INC., Tokyo, Japan) with a semiconductor laser (λ = 488 nm) were used to record the chemical binding energies and vibration modes of the chemical bonds. The surface morphology and EDS spectra of the pristine Bi_2Se_3 and $Ag@Bi_2Se_3$ nanoplatelets were obtained using FESEM (ZEISS Ultra Plus, Carl Zeiss Microscopy GmbH, Oberkochen, Germany). The optical absorptance of UV and visible light was recorded using a UV-visible spectrometer (Hitachi U3900-H, Hitachi Ltd., Tokyo, Japan) that was equipped with an integrating sphere.

2.3. Photocurrent Measurements

A semiconductor I-V characterizing analyzer (Keysight B2901A Precision Source/Measure Unit 100 fA, Keysight Technologies, Santa Rosa, CA, USA) recorded the photocurrents at 0 V bias under UV- and visible-light in the ambient environment. The sources of incident light were 30 cm-long UV (8 W, λ = 365 nm) and visible light (8 W, λ = 380–780 nm) LED lamps at 20 cm from the sample. The photocurrents in all samples were recorded in a dark room to eliminate any effect from stray lights. Silver paste was used as an electrode that was connected to a current analyzer using copper wires. The photocurrent in each sample was measured six times; each time, the light was on for 10 s and off for 10 s.

3. Results

3.1. XPS Analysis

Figure 1 present the XPS spectra of the Bi 4f, Se 3d, and Ag 3d of the pristine and $Ag25s@Bi_2Se_3$ nanoplatelets. Figure 1a display the spectra of the Bi 4f orbit of the pristine Bi_2Se_3 and $Ag25s@Bi_2Se_3$ nanoplatelets, revealing four significant peaks. The peaks at 157.94 and 163.26 eV are associated with the Bi $4f^{7/2}$ and Bi $4f^{5/2}$ in Bi_2Se_3 [16]; those at 158.69 and 164.30 eV correspond to the binding energies of the Bi–O phase in Bi_2O_3 [37]. Figure 1b show the XPS of Bi 4f in the pristine Bi_2Se_3 and $Ag25s@Bi_2Se_3$ nanoplatelets, from which the peaks are in similar positions. Figure 1c and d present the Se 3d orbits of the pristine Bi_2Se_3 and $Ag25s@Bi_2Se_3$ nanoplatelets. Three main peaks at 53.5, 54.3, and 55.1 eV are observed. The first two peaks correspond to Se $3d^{5/2}$ and Se $3d^{3/2}$ in Bi_2Se_3 [38], and the last one corresponds to the metal Se [39]. The metallic Se traps the free electrons and suppresses the photocurrent that arises from them. A weak peak at 58.66 eV is observed in Figure 1d, arising from the Se–O bonds [40]. These XPS spectra confirm the formation of the Bi_2Se_3 structure. The peaks of Bi–O and Se–O are attributed to natural formations on the surface of the sample in an ambient environment. Figure 1e present the Ag 3d binding energy in $Ag25s@Bi_2Se_3$ nanoplatelets. Peaks at 367.55 and 373.58 eV with an energy separation of 6.03 eV correspond to the Ag $3d^{5/2}$ and Ag $3d^{3/2}$ of metallic Ag. The binding energies of Ag $3d^{5/2}$ and Ag $3d^{3/2}$ are lower than that of bulk Ag (~368 eV). The shift of the binding energy is relative to the electronegativity of the elements and is responsible for the change in the charge around the atom [41]. The larger electronegativity of the element, the blue-shift of the binding energy. Ag (1.93) has a lower electronegativity than Bi (2.02) and Se (2.55). Therefore, the binding energies of Ag $3d^{5/2}$ and Ag $3d^{3/2}$ shift toward lower energy (red-shift). Table 1 show the atomic percentages of Bi, Se, and Ag, confirming the presence of Ag; the portion of Ag increases with the deposition time.

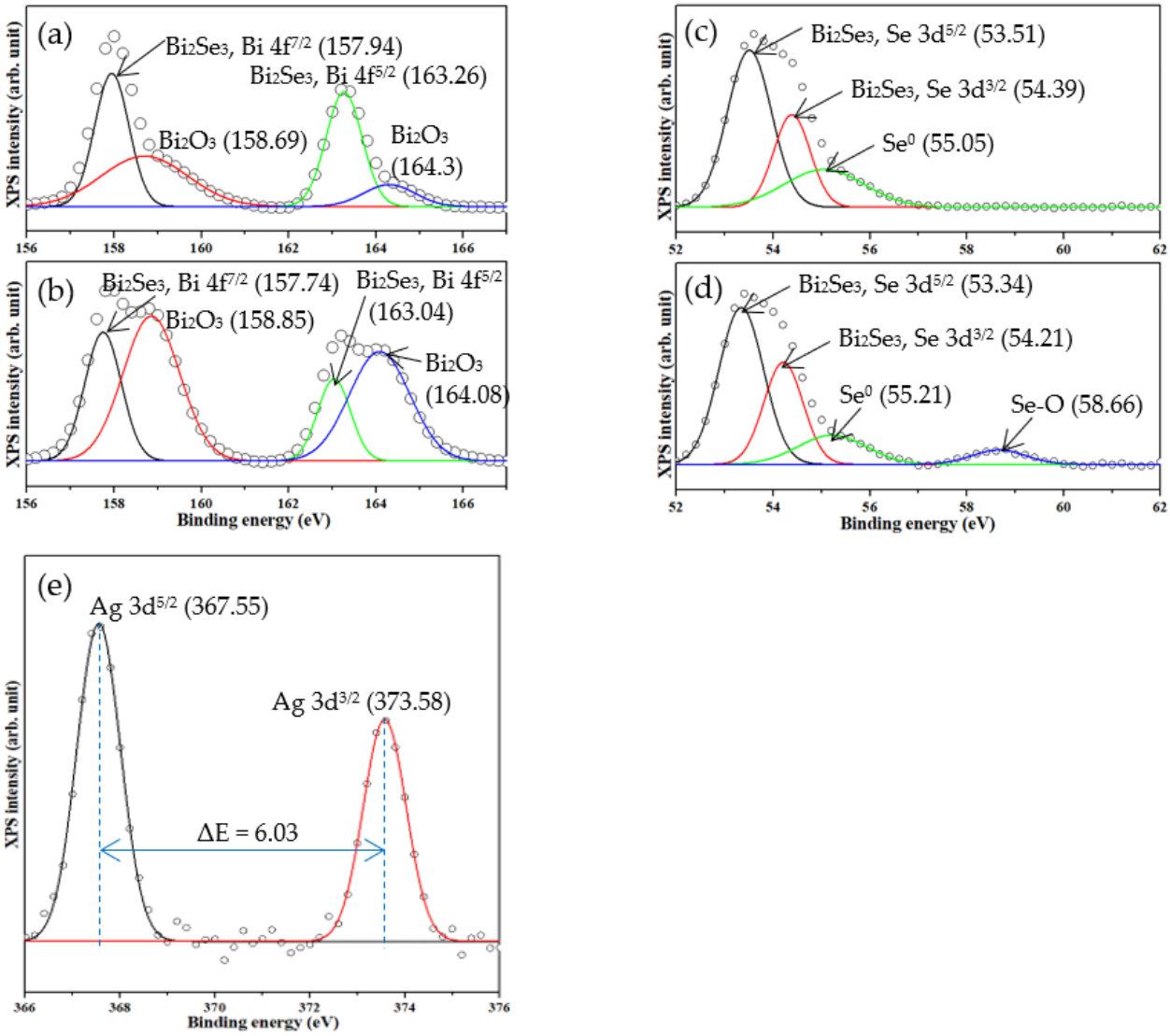

Figure 1. XPS spectra of Bi 4f, Se 3d of Bi_2Se_3 of (**a**,**c**), and of Ag25s@Bi_2Se_3 of (**b**,**d**); (**e**) Ag 3d of Ag25s@Bi_2Se_3 nanoplatelets.

Table 1. Atomic % of pristine Bi_2Se_3 and Ag@Bi_2Se_3 nanoplatelets of Bi, Se, and Ag.

Sample	Bi (at.%)	Se (at.%)	Ag (at.%)
Bi_2Se_3	47.1	52.9	0
Ag10s@Bi_2Se_3	52.3	42.3	5.3
Ag15s@Bi_2Se_3	53.5	41.1	5.4
Ag20s@Bi_2Se_3	53.5	39.4	7.1
Ag25s@Bi_2Se_3	52.6	39.2	8.2

3.2. Morphological Analysis

Figure 2a,b present the morphologies of the pristine Bi_2Se_3 and Ag25s@Bi_2Se_3 nanoplatelets that are obtained using FESEM. Both samples have a hexagonal structure which is typical of rhombohedral Bi_2Se_3. FESEM-EDS detects the presence of Ag along with the Bi and Se. The estimated thickness (40 nanoplatelets) and size (40 nanoplatelets) of each nanoplatelet of pristine Bi_2Se_3 is 6.9 and 8.3 nm; those of Ag25s@Bi_2Se_3 are 444.8 and 488.5nm, respectively. Bi_2Se_3 has the same layered structures as graphite. Each layer comprises five stacked atomic layers Se^1–Bi–Se^2–Bi–Se^1 and is called the quintuple layer (QL). The thickness of each QL is 0.955 nm [42], indicating that pristine Bi_2Se_3 and Ag25s@Bi_2Se_3

nanoplatelets have 7.22 and 8.69 OLs, respectively. Figure 2c present the thickness of the Ag thin film that is deposited on a sapphire substrate at 0.44W for 60s (110 V, 4 mA) at 1×10^{-1} mbar. The ideal Ag thicknesses in pristine Bi_2Se_3, Ag10s, Ag15s, Ag20s, and Ag25s@Bi_2Se_3 nanoplatelets are 0, 3.3, 5, 6.7, and 8.3 nm, respectively. Therefore, the Ag was not easily observed in the FESEM images.

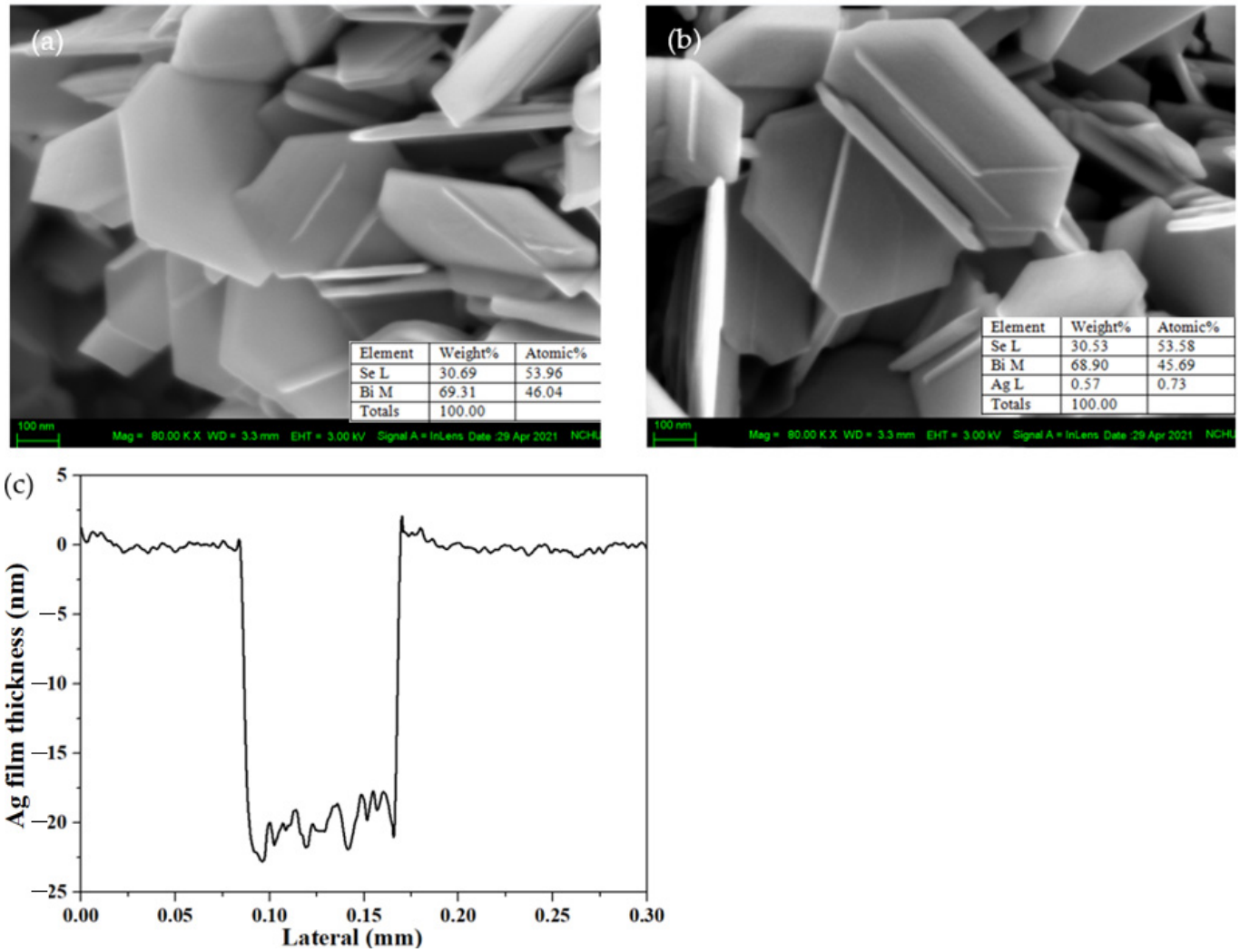

Figure 2. FESEM images of (**a**) Bi_2Se_3 and (**b**) Ag25s@Bi_2Se_3 nanoplatelets. Insets are the EDS results of Bi, Se, and Ag. (**c**) Thickness of Ag film deposits on the sapphire substrate.

3.3. Analysis of Crystal Structures and Surface Morphologies

Figure 3 present the XRD patterns of the pristine Bi_2Se_3 and Ag@Bi_2Se_3 nanoplatelets. Nine significant peaks are observed at 2θ values of 18.55°, 25.03°, 27.91°, 29.39°, 40.28°, 43.07°, 43.77°, 47.67°, and 53.61°, corresponding to the planes (006), (101), (104), (015), (10$\underline{1}$0), (01$\underline{1}$1), (110), (00$\underline{1}$5), and (205) of the rhombohedral Bi_2Se_3 structure (JCPDS 89-2008). No significant peak of oxides or silver are observed because the content of oxides and Ag are less than the limit of detection (~5%) by XRD. The grain sizes of pristine Bi_2Se_3 and Ag@Bi_2Se_3 nanoplatelets are estimated at 14.56±7.9% nm using the Williamson-Hall equation [43] and plotted in the inset in Figure 3. Table 2 present the lattice constants a (= b) and c and the c/a ratios of the Bi_2Se_3 nanoplatelets with various Ag contents.

Table 2. Lattice constants of a (= b) and c, and c/a ratios of Bi_2Se_3 nanoplatelets with various Ag contents.

Ag Contents (at.%)	a (= b) (nm)	c (nm)	c/a
0	0.4133	2.8675	6.9381
5.3	0.4129	2.8736	6.9595
5.4	0.4128	2.8721	6.9576
7.1	0.4129	2.8736	6.9595
8.2	0.4131	2.8705	6.9486

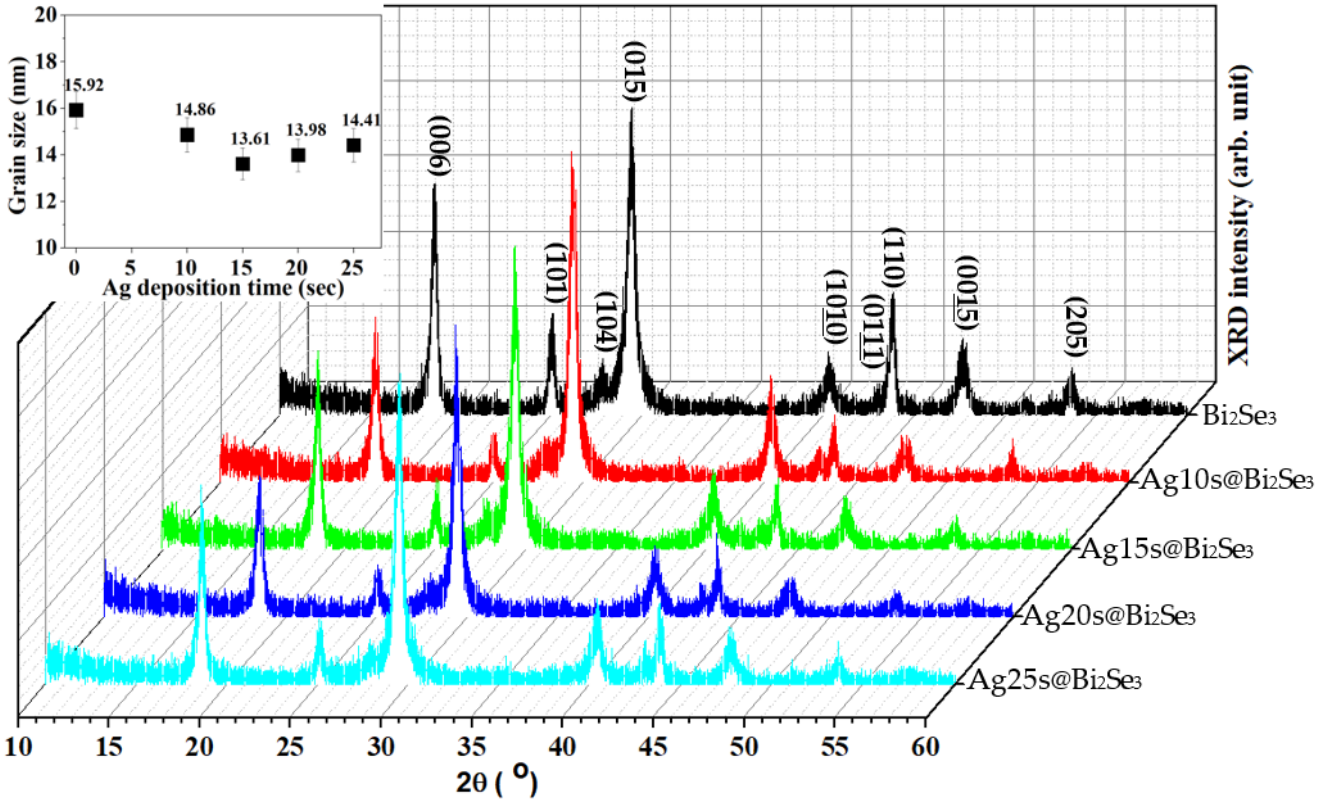

Figure 3. XRD patterns of Bi_2Se_3 and Ag@Bi_2Se_3 nanoplatelets. Inset are the grain size variations estimated by the W–H plot.

Figure 4a–c present the HRTEM images and selected area diffraction (SAD) patterns of the pristine Bi_2Se_3 nanoplatelets. Figure 4a present the hexagonal morphology that is typical of rhombohedral Bi_2Se_3. The d-spacings of 0.334 and 0.317 are estimated from Figure 4b, corresponding to the Bi_2Se_3 (012) and Bi_2Se_3 (009) planes. Figure 4c present the SAD patterns and reveals Bi_2Se_3 (101), Bi_2Se_3 (012), and Bi_2Se_3 (110) planes. Figure 4d–f present HRTEM images and SAD patterns of Ag25s@Bi_2Se_3 nanoplatelets. Figure 4d show that the Ag20s@Bi_2Se_3 nanoplatelets have the same morphology as the pristine ones, which is shown in Figure 4a. Figure 4e reveal the estimated d-spacings of 0.341 and 0.207 nm, which correspond to Bi_2Se_3 (012) and Ag (200), respectively, as shown in the blue-line region in Figure 4e. Figure 4f present the SAD pattern of Ag20s@Bi_2Se_3 nanoplatelets, which corresponds to the Bi_2Se_3 (012), Bi_2Se_3 (009), and Bi_2Se_3 (110) planes. The results of XRD and HRTEM reveal that the crystal structures of pristine Bi_2Se_3 and Ag20s@Bi_2Se_3 nanoplatelets are the typical rhombohedral Bi_2Se_3 structure. The Ag phase is also observed in Figure 4e.

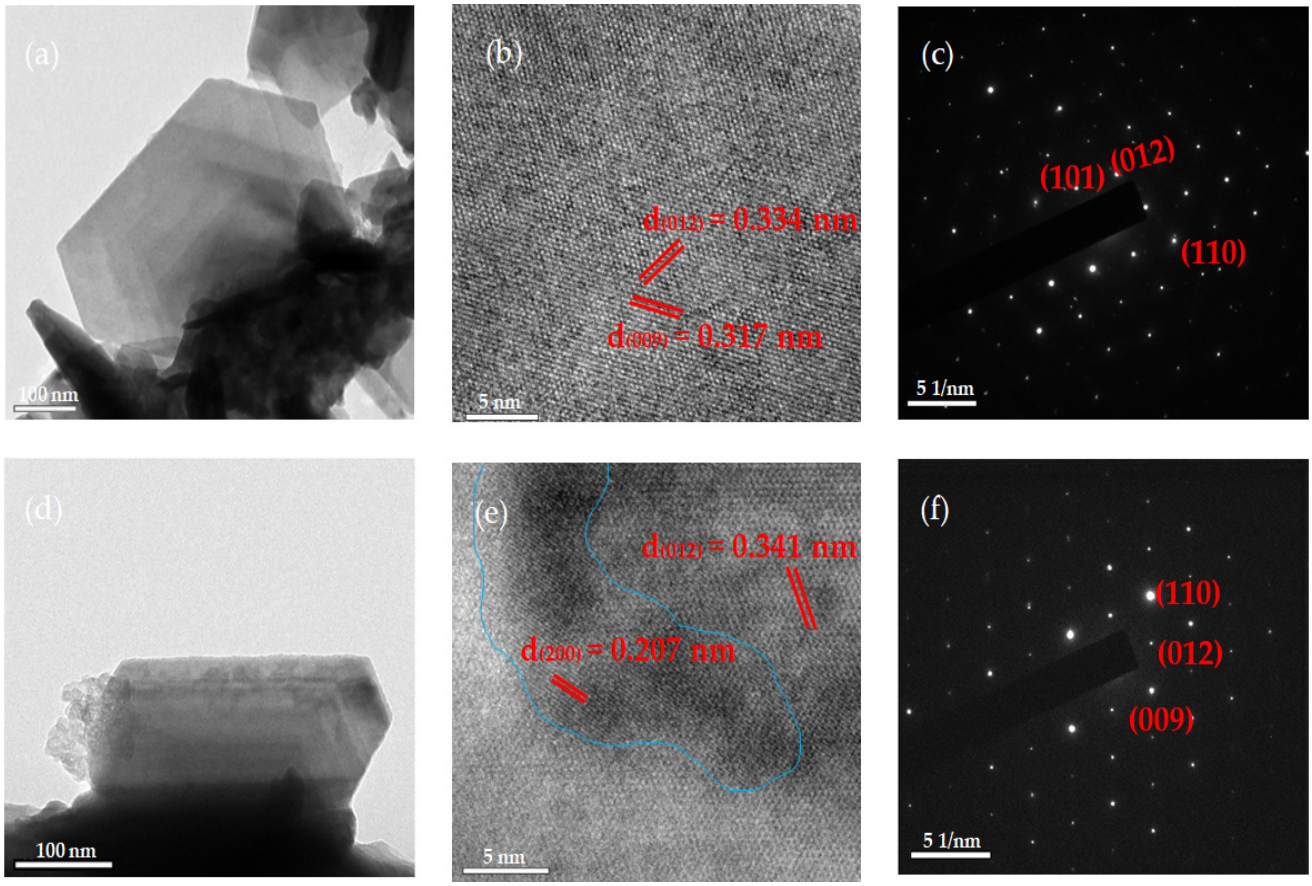

Figure 4. HRTEM images of (**a**,**b**) Bi_2Se_3 and (**d**,**e**) Ag20s@Bi_2Se_3; SAD patterns of (**c**) Bi_2Se_3 and (**f**) Ag20s@Bi_2Se_3 nanoplatelets.

3.4. Raman Analysis

Figure 5a,b present two typical Raman peaks of rhombohedral Bi_2Se_3 at E_g^2 and A_{1g}^2 from the pristine Bi_2Se_3 and Ag25s@Bi_2Se_3 nanoplatelets [16]. Bi_2Se_3 belongs to the space group ($R\bar{3}m/D_{3d}^5$). The atoms in a QL are bonded covalently [44]; Van der Waals forces bind the QLs [16]. The zone-center phonon formula of Bi_2Se_3 is $\chi = 2E_g + 2A_{1g} + 2E_u + 2A_{1u}$ [42], where $2A_{1g}$ and $2E_g$ are the Raman-active modes and $2A_{1u}$ and $2E_u$ are the infrared-active modes. The A_{1g}^2 mode is the out-of-plane stretching symmetry mode with the vibration of the Se^1 and Bi^1 atoms in opposite directions. Therefore, the A_{1g}^2 mode has a short displacement (Figure 5a). The E_g^2 mode is the in-plane bending symmetry mode shearing the upper Se^1 and Bi^1 atomic layers, which vibrate with a longer displacement than in the A_{1g}^2 mode and have a large binding energy (Figure 5a) [45]. These results suggest that the rhombohedral Bi_2Se_3 formed successfully, and the Ag has no significant effect on the binding structure.

3.5. Analysis of Optical Properties

Figure 6a present the absorptance spectrum of the pristine Bi_2Se_3 and Ag@Bi_2Se_3 nanoplatelets. The absorptance of the nanoplatelets decreases as the Ag deposition time increases. Figure S1 reveal the absorptance of Ag/Bi_2Se_3 thin film as simulated in TFCalc software. The simulation involves (1) a Bi_2Se_3 thin film with a thickness of 10 nm, (2) Ag thin films with a thickness of 0, 2, 4, 6, 8, and 10 nm, and (3) a sapphire substrate. The absorptance of the Ag@Bi_2Se_3 thin films decreases as the Ag thickness increases, consistent with the experimental results (Figure 6a). This decrease in absorptance is attributed to the increase in reflectance by the decoration with Ag. The absorptance of the Ag@Bi_2Se_3 nanoplatelets is therefore suppressed. Figure 6b present the normalized absorptance at

various Ag deposition times. The Ag@Bi_2Se_3 nanoplatelets have a broad band from 375 to 420 nm that is centered at ~398 nm.

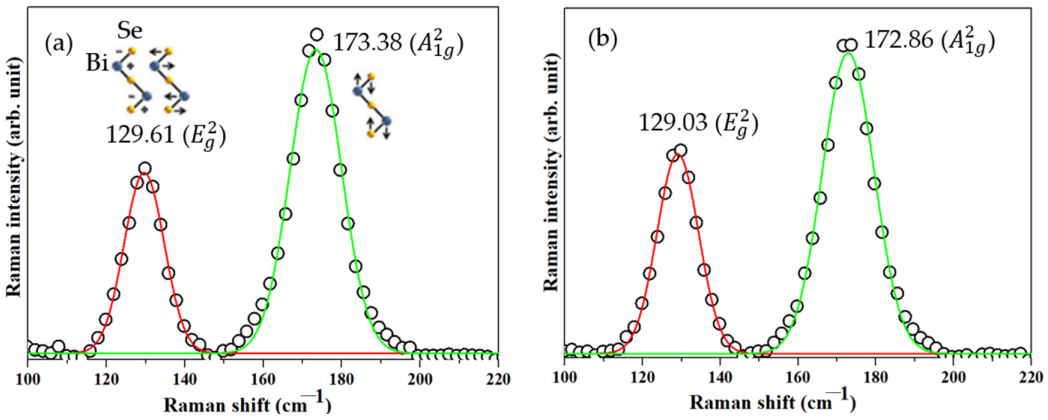

Figure 5. Raman spectra of (**a**) Bi_2Se_3 and (**b**) Ag25s@Bi_2Se_3 nanoplatelets.

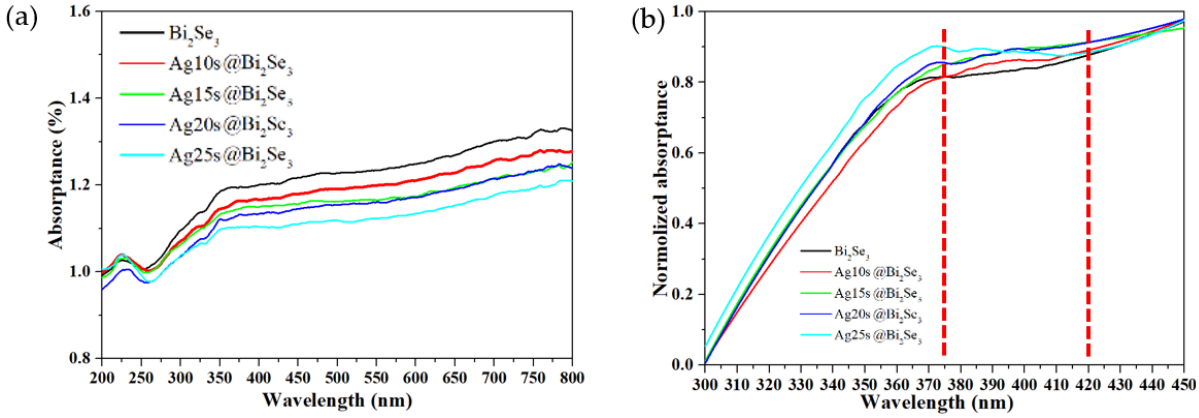

Figure 6. (**a**) UV-visible absorptance and (**b**) normalization of absorptance of pristine Bi_2Se_3 and Ag@Bi_2Se_3 nanoplatelets.

In order to understand the effect of the Ag thin film on the optical absorptance of Bi_2Se_3, a simulation is performed, and its results are presented in Figure S2. The simulated structure is a Au thin film/Bi_2Se_3 thin film (10 nm)/sapphire substrate. The simulation involves (1) Ag thin films with a thickness of 0, 2, 4, 6, 8, and 10 nm, and (2) a sapphire substrate. A significant peak at 400 nm is observed while the Ag thickness increases, as shown in Figure S2, consistent with the experimental results (Figure 6b). The broad peak from 375 to 420 nm that is centered at ~398 nm (Figure 6b) is therefore confirmed to be caused by the Ag and attributable to the surface plasmon resonance [46].

3.6. Photocurrent under the UV and Visible Light

Figure 7a,b plot the measured photocurrents under UV (8 W, λ = 365 nm) and visible light (8 W, λ = 380–780 nm); the measurements are performed six times. Each measurements cycle lasts 20 s, comprising 10 s under illumination and 10 s without illumination. The substrate bias is 0 voltage during the measurement of photocurrent; therefore, the photocurrents are spontaneously generated by the incident light. The photocurrents in pristine Bi_2Se_3 under UV and visible light are lower than those in the Ag@Bi_2Se_3 nanoplatelets, as shown in Figure 7a,b. The photocurrent increases with Ag content from 0 to 7.1 at.%, and then decreases as the Ag content increases further to 8.2 at.%. Figure 7c plot the photocurrent as a function of Ag content. The highest photocurrents at 7.1 at.% Ag exceed those in the pristine nanoplatelets by factors about 4.25 and 4.57 under UV and visible light, respectively. Additionally, the photocurrents at 7.1 at.% Ag under visible light exceed those under UV light by a factor of about 1.7. These results reveal that a particular Ag

content can increase the photocurrent in Bi_2Se_3 nanoplatelets under UV and visible light and that Ag@Bi_2Se_3 nanoplatelets have higher photosensitivity under visible light than that under UV light.

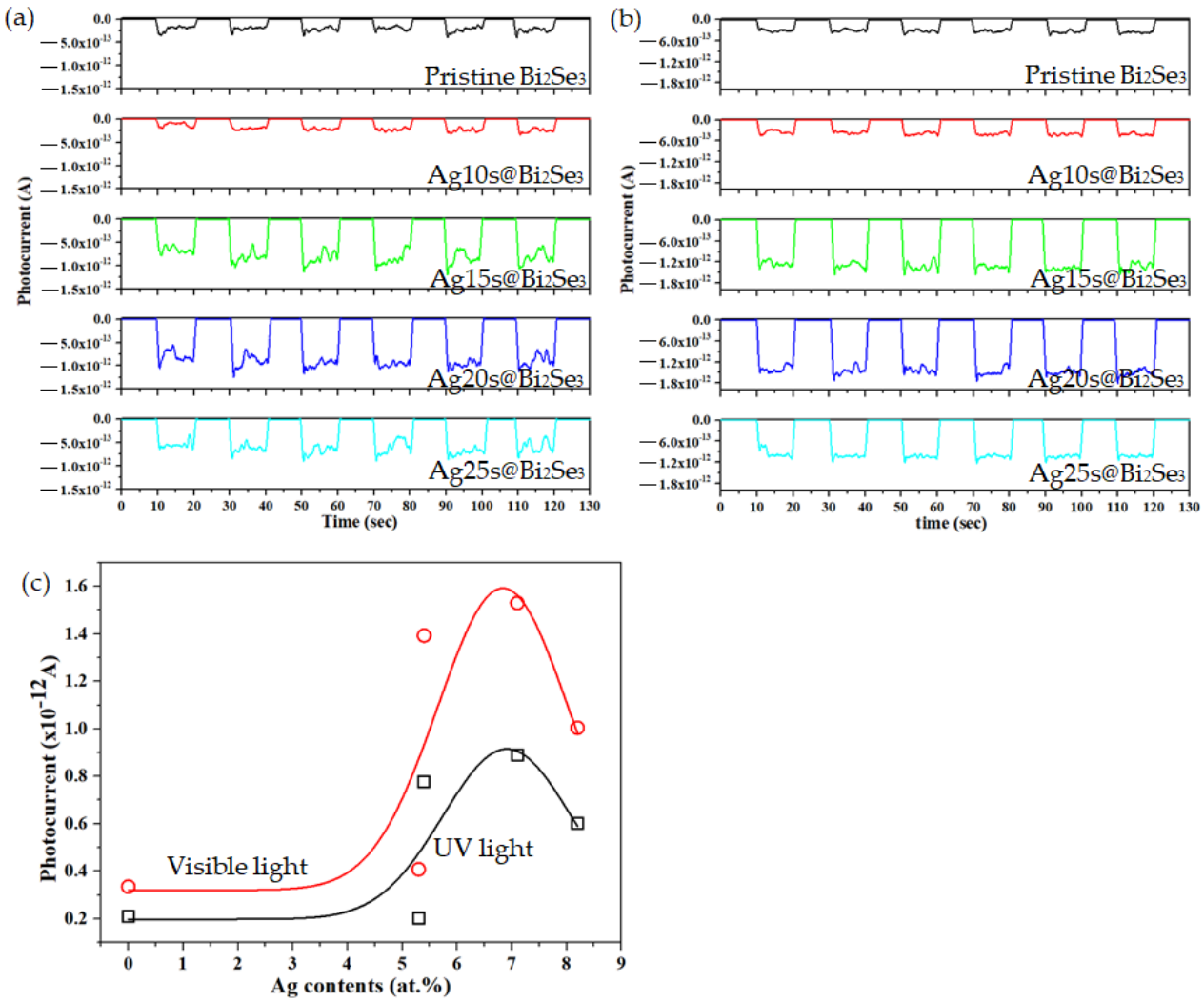

Figure 7. Photocurrents versus measured time under (**a**) UV, (**b**) visible light and (**c**) The variations of the photocurrent versus Ag contents (at.%).

3.7. Mechanism of Photocurrent Enhancement

Bi_2Se_3 is a semiconductor with a narrow bandgap (~0.35 eV) [47], in which the photo-induced electron-hole pairs are readily generated by UV and visible light. A Schottky field can be formed at the interface between Ag and Bi_2Se_3, and it dissociates the photo-induced electrons and holes in Bi_2Se_3 [29]. This dissociation process generates free electrons and suppresses their recombination with holes. Surface plasmon resonance (SPR) (Figure 6b) is observed in the Ag@Bi_2Se_3 nanoplatelets. SPR is the collective oscillation of electrons in the conduction band after the absorption of light with a particular incident energy, generating unstable/free electrons. These free electrons can be smoothly transported at the conductive surface that contributed to the Ag and nanosized Bi_2Se_3 platelets [15], enhancing the photocurrent. This photocurrent enhancement has the following causes: (1) the narrow bandgap of the pristine Bi_2Se_3 nanoplatelets, (2) the Schottky field at the interface between Ag and Bi_2Se_3, (3) the SPR effect of the Ag decoration, and (4) the highly conductive surface contributing to the Ag and Bi_2Se_3 nanoplatelets. Figure 8 present the proposed transmission path.

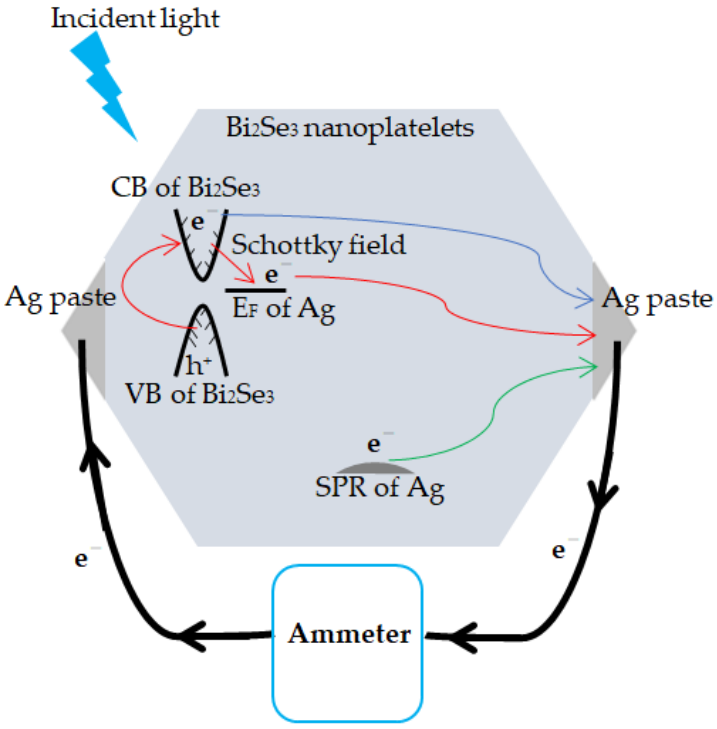

Figure 8. The proposed transmission path of electrons in the Ag@Bi_2Se_3 nanoplatelets.

Notably, the photocurrent under visible light exceeds that under UV. The absorptance of nanoplatelets under visible light exceeds that under UV (Figure 6a), indicating that visible light can be efficiently used by the nanoplatelets. The high-energy incident light (UV) generates high concentrations of free carriers close to the surface. These free carriers then recombine through surface states because of the high carrier density, reducing the total photocurrent [48]. A high Ag content (8.1 at.%) is associated with lower photocurrent under UV or visible light. The SPR enhances the near-field intensity and increases the concentrations of unstable/free electrons. Therefore, higher densities of electrons are generated in the surface region, and these electrons subsequently recombine with the holes, suppressing the photocurrent.

4. Conclusions

The Ag@Bi_2Se_3 nanoplatelets exhibit a significantly higher photocurrent under UV and visible light. The photocurrents of Ag@Bi_2Se_3 nanoplatelets with 7.1 at.% Ag under UV and visible light were approximately 4.25 and 4.57 times larger than those in pristine Bi_2Se_3 nanoplatelets. The resulting photocurrent in the Ag@Bi_2Se_3 nanoplatelets with 7.1 at.% Ag under visible light is 1.72-fold compared to that of pristine nanoplatelets under UV light. The presence of Ag and metallic Se is confirmed by XPS, FESEM, and HRTEM images. Free electrons are trapped by metallic Se, reducing the photocurrent. The rhombohedral Bi_2Se_3 crystal structure is confirmed by XRD, HRTEM, and Raman spectra. The Ag decoration has no effect on the Bi_2Se_3 crystal structure. The absorptance that is recorded by the UV-visible spectrometer reveals that increasing the Ag content reduces their total absorptance, affecting their light-to-electron transformation efficiency, suppressing the generation of the photocurrent. The SPR effect of Ag is evident in the absorptance spectra; it generates unstable/free electrons, enhancing the photocurrent in the nanoplatelets. The appropriate Ag content significantly enhances the photocurrent of pristine Bi_2Se_3 nanoplatelets because of the following: (1) the narrow bandgap of Bi_2Se_3 nanoplatelets, (2) the Schottky field at the interface between Ag and Bi_2Se_3, (3) the surface plasmon resonance that is caused by Ag, and (4) the highly conductive surface. The photocurrent was suppressed for the following reasons: (1) the high carrier densities that are generated by the high-energy incident light and SPR increase

the rate of recombination between electrons and holes; (2) metallic Se may act as a recombination center; and (3) the absorptance of the Bi_2Se_3 nanoplatelets is reduced by Ag decoration. This work suggests that the incorporation of a particular amount of Ag enhances the photocurrent in Ag@Bi_2Se_3 nanoplatelets; this phenomenon may have immediate application in the detection of UV and visible light.

Supplementary Materials: The following are available online at https://www.mdpi.com/article/10.3390/nano11123353/s1, Figure S1: (a–f) are the simulated absorptance spectra of the Ag@Bi_2Se_3 thin film while Ag thin film at 0, 2, 4, 6, 8, and 10 nm, Figure S2: (a–f) are the simulated absorptance spectra of Ag thin film in 0, 2, 4, 6, 8, and 10 nm.

Author Contributions: Conceptualization, F.-S.S. and H.-C.S.; methodology, F.-S.S., H.-C.S., P.-T.L. and C.-C.W.; software, C.-C.W.; validation, C.-C.W.; formal analysis, C.-C.W. and P.-T.L.; investigation, C.-C.W.; resources, H.-C.S. and F.-S.S.; data curation, C.-C.W. and P.-T.L.; writing—original draft preparation, C.-C.W.; writing-review and editing, P.-T.L., H.-C.S. and F.-S.S.; visualization, C.-C.W.; supervision, H.-C.S. and F.-S.S.; project administration, H.-C.S.; funding acquisition, H.-C.S. All authors have read and agreed to the published version of the manuscript.

Funding: This research was funded by the Ministry of Science and Technology (MOST) of Taiwan, Republic of China, grant number MOST 110-2221-E-034-006, and the Higher Education Sprout Project (HESP), Ministry of Education (MOE), Taiwan, R.O.C under the contract 110S0802C.

Institutional Review Board Statement: Not applicable.

Informed Consent Statement: Not applicable.

Data Availability Statement: Data is contained within the article.

Acknowledgments: The authors gratefully acknowledge the financial support of the Ministry of Science and Technology (MOST) of Taiwan, Republic of China, and the Higher Education Sprout Project (HESP), Ministry of Education (MOE), Taiwan, R.O.C.

Conflicts of Interest: The authors declare no conflict of interest.

References

1. Nechaev, I.A. Evidence for a direct band gap in the topological insulator Bi_2Se_3 from theory and experiment. *Phys. Rev. B Condens. Matter Mater. Phys.* **2013**, *87*, 121111. [CrossRef]
2. Liu, X.; Xu, J.; Fang, Z.; Lin, L.; Qian, Y.; Wang, Y.; Ye, C.; Ma, C.; Zeng, J. One-pot synthesis of Bi_2Se_3 nanostructures with rationally tunable morphologies. *Nano Res.* **2015**, *8*, 3612–3620. [CrossRef]
3. Kane, C.L.; Mele, E.J.Z. Topological order and the quantum spin Hall effect. *Phys. Rev. Lett.* **2005**, *95*, 146802. [CrossRef] [PubMed]
4. Konig, M.; Wiedmann, S.; Brune, C.; Roth, A.; Buhmann, H.; Molenkamp, L.W.; Qi, X.L.; Zhang, S.C. Quantum spin Hall insulator state in HgTe quantum wells. *Science* **2007**, *318*, 766–770. [CrossRef] [PubMed]
5. Irfan, B.; Sahoo, S.; Gaur, A.P.S.; Ahmadi, M.; Guinel, M.J.F.; Katiyar, R.S.; Chatterjee, R. Temperature dependent Raman scattering studies of three dimensional topological insulators Bi_2Se_3. *J. Appl. Phys.* **2014**, *115*, 173506. [CrossRef]
6. Fei, F.; Zhang, S.; Zhang, M.; Shah, S.A.; Song, F.; Wang, X.; Wang, B. The material efforts for quantized Hall devices based on topological insulators. *Adv. Mater.* **2020**, *32*, 1904593. [CrossRef]
7. Mishra, S.K.; Satpathy, S.; Jepsen, O. Electronic structure and thermoelectric properties of bismuth telluride and bismuth selenide. *J. Phys. Condens. Matter.* **1997**, *9*, 461–470. [CrossRef]
8. Tian, W.; Yu, W.; Shi, J.; Wang, Y. The property, preparation and application of topological insulators: A review. *Materials* **2017**, *10*, 814. [CrossRef]
9. Wang, F.; Li, L.; Huang, W.; Li, L.; Jin, B.; Li, H.; Zhai, T. Submillimeter 2D Bi2Se3 flakes toward high-performance infrared photodetection at optical communication wavelength. *Adv. Funct. Mater.* **2018**, *28*, 1802707. [CrossRef]
10. Tian, J.; Şahin, C.; Miotkowski, I.; Flatté, M.E.; Chen, Y.P. Opposite current-induced spin polarizations in bulk-metallic Bi_2Se_3 and bulk-insulating Bi_2Te_2Se topological insulator thin flakes. *Phys. Rev. B* **2021**, *103*, 035412. [CrossRef]
11. Kong, P.P.; Zhang, J.L.; Zhang, S.J.; Zhu, J.; Liu, Q.Q.; Yu, R.C.; Fang, Z.; Jin, C.Q.; Yang, W.G.; Yu, X.H.; et al. Superconductivity of the topological insulator Bi_2Se_3 at high pressure. *J. Phys. Condens. Matter* **2013**, *25*, 362204. [CrossRef] [PubMed]
12. Yonezawa, S. Nematic superconductivity in doped Bi_2Se_3 topological superconductors. *Condens. Matter* **2019**, *4*, 2. [CrossRef]
13. Kim, D.; Cho, S.; Butch, N.P.; Syers, P.; Kirshenbaum, K.; Adam, S.; Paglione, J.; Fuhrer, M.S. Surface conduction of topological Dirac electrons in bulk insulating Bi_2Se_3. *Nat. Phys.* **2012**, *8*, 459–463. [CrossRef]
14. Jia, S.; Beidenkopf, H.; Drozdov, I.; Fuccillo, M.K.; Seo, J.; Xiong, J.; Ong, N.P.; Yazdani, A.; Cava, R.J. Defects and high bulk resistivities in the Bi-rich tetradymite topological insulator Bi_2+xTe_2−xSe. *Phys. Rev. B* **2012**, *86*, 165119. [CrossRef]

15. Schönherr, P.; Collins-McIntyre, L.J.; Zhang, S.; Kusch, P.; Reich, S.; Giles, T.; Daisenberger, D.; Prabhakaran, D.; Hesjedal, T. Vapour-liquid-solid growth of ternary Bi_2Se_2Te nanowires. *Nanoscale Res. Lett.* **2014**, *9*, 127. [CrossRef]
16. Wang, C.C.; Shieu, F.S.; Shih, H.C. Photosensing and characterizing of the pristine and In-, Sn-doped Bi_2Se_3 nanoplatelets fabricated by thermal V–S process. *Nanomaterials* **2021**, *11*, 1352. [CrossRef]
17. Ahmed, R.; Xu, Y.; Sales, M.G.; Lin, Q.; McDonnell, S.; Zangari, G. Synthesis and material properties of Bi_2Se_3 nanostructures deposited by SILAR. *J. Phys. Chem. C* **2018**, *122*, 12052–12060. [CrossRef]
18. Wang, W.; Wang, X.; Wang, N.; Ning, X.; Li, H.; Lu, D.; Liu, X.; Zhang, Q.; Huang, Y. Bi_2Se_3 sensitized TiO2 nanotube films for photogenerated cathodic protection of 304 stainless steel under visible light. *Nanoscale Res. Lett.* **2018**, *13*, 295. [CrossRef] [PubMed]
19. Souza, P.B.; Tumelero, M.A.; Zangari, G.; Pasa, A.A. Tuning electrodeposition conditions towards the formation of smooth Bi_2Se_3 thin films. *J. Electrochem. Soc.* **2017**, *164*, D401–D405. [CrossRef]
20. Liang, K.; Wang, C.; Xu, X.; Leng, J.; Ma, H. Capacitive and photocatalytic performance of Bi_2Se_3 nanostructures synthesized by solvothermal method. *Phys. Lett. A* **2017**, *381*, 652–657. [CrossRef]
21. Li, X.M.; Zhao, K.; Ni, H.; Zhao, S.Q.; Xiang, W.F.; Lu, Z.Q.; Yue, Z.J.; Wang, F.; Kong, Y.C.; Wong, H.K. Voltage tunable photodetecting properties of La0.4Ca0.6MnO3 films grown on miscut $LaSrAlO_4$ substrates. *Appl. Phys. Lett.* **2010**, *97*, 044104. [CrossRef]
22. Huang, S.M.; Huang, S.J.; Yan, Y.J.; Yu, S.H.; Chou, M.; Yang, H.W.; Chang, Y.S.; Chen, R.S. Extremely high-performance visible light photodetector in the Sb2SeTe2 nanoflake. *Sci. Rep.* **2017**, *7*, 45413. [CrossRef]
23. Sharma, A.; Bhattacharyya, B.; Srivastava, A.K.; Senguttuvan, T.D.; Husale, S. High performance broadband photodetector using fabricated nanowires of bismuth selenide. *Sci. Rep.* **2016**, *6*, 19138. [CrossRef]
24. Bhattacharyya, B.; Sharma, A.; Kaur, M.; Singh, B.P.; Husale, S. Highly responsive broadband photodetection in topological insulator-Carbon nanotubes based heterostructure. *J. Alloys Compd.* **2021**, *851*, 156759. [CrossRef]
25. Zhang, H.; Song, Z.; Li, D.; Xu, Y.; Li, J.; Bai, C.; Man, B. Near-infrared photodetection based on topological insulator P-N heterojunction of SnTe/ Bi2Se3. *Appl. Surf. Sci.* **2020**, *509*, 145290. [CrossRef]
26. Pamu, R.; Lawrie, B.J.; Khomami, B.; Mukherjee, D. Broadband plasmonic photocurrent enhancement from photosystem I assembled with tailored arrays of Au and Ag nanodisks. *ACS Appl. Nano Mater.* **2021**, *4*, 1209–1219. [CrossRef]
27. Peng, K.; Wu, S.; Xie, X.; Yang, J.; Qian, C.; Song, F.; Sun, S.; Dang, J.; Yu, Y.; Shi, S.; et al. Giant photocurrent enhancement by coulomb interaction in a single quantum dot for energy harvesting. *Phys. Rev. Appl.* **2019**, *11*, 024015. [CrossRef]
28. Yan, W.; Tao, Z.; Gu, M.; Richards, B.S. Photocurrent enhancement of ultrathin front-textured crystalline silicon solar cells by rear-located periodic silver nanoarrays. *Sol. Energy* **2017**, *150*, 156–160. [CrossRef]
29. Chakraborty, R.; Greullet, F.; George, C.; Baranov, D.; Fabrizio, E.D.; Krahne, R. Broad spectral photocurrent enhancement in Au-decorated CdSe nanowires. *Nanoscale* **2013**, *5*, 5334. [CrossRef]
30. Meyer, N.; Geishendorf, K.; Walowski, J.; Thomas, A.; Munzenberg, M. The impact of metallic contacts on spin-polarized photocurrents in topological insulator Bi_2Se_3 nanowires. *Appl. Phys. Lett.* **2020**, *117*, 262401. [CrossRef]
31. Hong, X.; Shen, J.; Tang, X.; Xie, Y.; Su, M.; Tai, G.; Yao, J.; Fu, Y.; Ji, J.; Liu, X.; et al. High-performance broadband photodetector with in-situ-grown Bi_2Se_3 film on micropyramidal Si substrate. *Opt. Mater.* **2021**, *117*, 111118. [CrossRef]
32. Xiao, L.; Liu, Q.; Zhang, M.; Liu, L. Photoelectric properties of Bi2Se3 films grown by thermal evaporation method. *Mater. Res. Express* **2020**, *7*, 016429. [CrossRef]
33. Wang, X.; Dai, G.; Liu, B.; Zou, H.; Chen, Y.; Mo, X.; Li, X.; Sun, J.; Liu, Y.; Liu, Y.; et al. Broadband photodetectors based on topological insulator Bi_2Se_3 nanowire with enhanced performance by strain modulation effect. *Phys. E Low-Dimens. Syst. Nanostruct.* **2019**, *114*, 113620. [CrossRef]
34. Gupta, A.; Chowdhury, R.K.; Ray, S.K.; Srivastava, S.K. Selective photoresponse of plasmonic silver nanoparticle decorated Bi_2Se_3 nanosheets. *Nanotechnology* **2019**, *30*, 435204. [CrossRef] [PubMed]
35. Chae, J.; Hong, S.B.; Kim, D.; Kim, D.K.; Kim, J.; Jeong, K.; Park, S.H.; Cho, M.H. Enhancement of photoresponse in Bi_2Se_3/graphene heterostructures by effective electron—Hole separation through internal band bending. *Appl. Surf. Sci.* **2021**, *554*, 149623. [CrossRef]
36. Liao, G.; Zhou, Y.; Huang, Z.; Ma, Q.; Luo, S.; Liu, Y.; Qi, X. Bi_2Se_3 nanosheets hybridized with reduced graphene oxide for enhanced photoelectrochemical activity. *Appl. Phys. A* **2021**, *127*, 705. [CrossRef]
37. Meng, A.; Yuan, X.; Shen, T.; Li, Z.; Jiang, Q.; Xue, H.; Lin, Y.; Zhao, J. One-step synthesis of flower-like Bi_2O_3/Bi_2Se_3 nanoarchitectures and $NiCoSe_2$/Ni0.85Se nanoparticles with appealing rate capability for the construction of high-energy and long-cycle-life asymmetric aqueous batteries. *J. Mater. Chem. A* **2019**, *7*, 17613. [CrossRef]
38. Zhang, G.; Qin, H.; Teng, J.; Guo, J.; Guo, Q.; Dai, X.; Fang, Z.; Wu, K. Quintuple-layer epitaxy of thin films of topological insulator Bi_2Se_3. *Appl. Phys. Lett.* **2009**, *95*, 053114. [CrossRef]
39. Wagner, C.D.; Riggs, W.M.; Davis, L.E.; Moulder, J.F.; Muilenberg, G.E. *Hand Book of X-ray Photoelectron Spectroscopy*; Perkin-Elmer Corporation: Eden Prairie, MN, USA, 1979; p. 92.
40. Hobbs, R.G.; Schmidt, M.; Bolger, C.T.; Georgiev, Y.M.; Fleming, P.; Morris, M.A.; Petkov, N.; Holmes, J.D.; Xiu, F.; Wang, K.L.; et al. Resist–substrate interface tailoring for generating high-density arrays of Ge and Bi_2Se_3 nanowires by electron beam lithography. *J. Vac. Sci. Technol. B* **2012**, *30*, 041602. [CrossRef]

41. Lamb, R.N.; Ngamsom, B.; Trimm, D.L.; Gong, B.; Silveston, P.L.; Praserthdam, P. Surface characterisation of Pd–Ag/Al_2O_3 catalysts for acetylene hydrogenation using an improved XPS procedure. *Appl. Catal. A-Gen.* **2004**, *268*, 43–50. [CrossRef]
42. Zhang, J.; Peng, Z.; Son, A.; Zhao, Y.; Xiong, Y.; Peng, B.; Wang, J.; Dresselhaus, M.S.; Xiong, Q. Raman spectroscopy of few-quintuple layer topological insulator Bi_2Se_3 nanoplatelets. *Nano Lett.* **2011**, *11*, 2407–2414. [CrossRef] [PubMed]
43. Mote, V.D.; Purushotham, Y.; Dole, B.N. Williamson-Hall analysis in estimation of lattice strain in nanometer-sized ZnO particles. *J. Theor. Appl. Phys.* **2012**, *6*, 6. [CrossRef]
44. Zhang, M.; Liu, L.G.; Wang, D.; An, X.Y.; Yang, H. Enhancement of surface state contribution in cadmium doped Bi_2Se_3 single crystal. *J. Alloys Compd.* **2019**, *806*, 180–186. [CrossRef]
45. Yuan, J.; Zhao, M.; Yu, W.; Lu, Y.; Chen, C.; Xu, M.; Li, S.; Loh, K.P.; Bao, Q. Raman spectroscopy of two-dimensional Bi_2TexSe_3–x platelets produced by solvothermal method. *Materials* **2015**, *8*, 5007–5017. [CrossRef] [PubMed]
46. Gharibshahi, L.; Saion, E.; Gharibshahi, E.; Shaari, A.H.; Matori, K.A. Structural and optical properties of Ag nanoparticles synthesized by thermal treatment method. *Materials* **2017**, *10*, 402. [CrossRef] [PubMed]
47. Lawal, A.; Shaari, A.; Ahmed, R.; Jarkoni, N. First-principles many-body comparative study of Bi_2Se_3 crystal: A promising candidate for broadband photodetector. *Phys. Lett. A* **2017**, *381*, 2993–2999. [CrossRef]
48. Ba, X.J.; Schlesinger, T.E.; James, R.B. Chapter 4-Electrical properties of mercuric iodide. In *Semiconductors and Semimetals: A Treatise*; Willardson, R.K., Beer, A.C., Weber, E.R., Eds.; Academic Press: Millbrae, CA, USA, 1995; Volume 43, pp. 111–168.